Arch Computat Methods Eng (2014) 21:273–292
DOI 10.1007/s11831-014-9105-0

How Constitutive Model Complexity can Affect the Capability to Fit Experimental Data: a Focus on Human Carotid Arteries and Extension/Inflation Data

F. Auricchio · M. Conti · A. Ferrara

Published online: 20 May 2014

Abstract To perform realistic finite element simulations of cardiovascular surgical procedures (such as balloon angioplasty, stenting or bypass), it is necessary to use appropriate constitutive models able to describe the mechanical behavior of the human arterial wall (in healthy and diseased conditions) as well as to properly calibrate the material parameters involved in such constitutive models. Moving from these considerations, the goal of the present study is to compare the reliability of two isotropic phenomenological models and of four structural invariant-based constitutive models, commonly used to describe the passive mechanical behavior of arteries. The arterial wall is modeled as a thick-wall tube with one- and two- layer structure. Residual stresses inclusion is also considered, to evaluate informations on the stress distribution through the wall thickness. The predictive capability of the investigated models is tested using extension/inflation data on human carotid arteries related by two different experimental works available in the literature. The material parameters involved in the investigated models are computed in the least-square sense thought a best fitting procedure, relying on a multi-start optimization algorithm. The good quality of the optimal solution is validated quantitatively computing proper error measures and comparing the model prediction curves. The final outcome of the paper is a critical review of the six considered constitutive models, comparing their formulation and evidencing the more or less capability of such models to fit the considered experimental data.

F. Auricchio · M. Conti · A. Ferrara (✉)
Dipartimento di Ingegneria Civile e Architettura (DICAr), Università degli Studi di Pavia, Via Ferrata 1, Pavia 27100 , Italy
e-mail: anna.ferrara@unipv.it

F. Auricchio
Istituto di Matematica Applicata e Tecnologie Informatiche "Enrico Magenes" (IMATI), CNR, Pavia, Italy

F. Auricchio
Centro di Simulazione Numerica Avanzata (CeSNA), IUSS, Pavia, Italy

1 Introduction

Cardiovascular diseases (such as atherosclerosis and aneurysm) are nowadays the leading cause of death in Europe, accounting for over 4.35 million deaths each year [1–3]. The development of such diseases involves significant changes in the arterial tissue from the histological point of view and, as consequence, may induce a different mechanical behavior of such a tissue with respect to healthy conditions. Accordingly, the identification of arterial mechanical properties can be of paramount importance for clinical diagnoses and treatments. In fact, on one hand, the knowledge of human arterial mechanical properties can provide helpful information to predict the onset and the progression of atherosclerotic lesions [4–6], the rupture of aneurysm [7,8] as well as to design artificial vascular grafts [9]. On the other hand, such a knowledge is essential to study and to optimize the performance of minimally-invasive interventions (such as balloon angioplasty or stenting) through finite element simulations [6,10–14]. In this context, a vascular district of particular clinical importance is the carotid bifurcation due to the very high incidence of the previous mentioned pathologies as well as to the district geometrical complexity, which demands for advanced computational modeling.

For accurately predicting stress/strain distributions as well as the interventions outcome, one promising approach is to use finite element analysis with patient-specific geometrical models, generated from imaging data, and with appropriate constitutive models, able to describe the mechanical behavior of the human arterial wall (in both healthy and diseased conditions). Moving from these considerations, in this work

we focus on the constitutive modeling feature, which is a very active field of research continuously increasing in the biomechanics area.

Within the framework of nonlinear hyper-elasticity [15] and invariant theory [16,17], two major groups of constitutive models may be evidenced, i.e.: (i) the *isotropic phenomenological approach* [18–23]; and (ii) the more recent *structural invariant- approach* [24–28,46]. The two formulations principally differ for the more or less ability to take into account the histological evidences on the arterial wall tissue and then, to capture the incompressible, anisotropic and nonlinear stiffen behavior of arteries. In particular *phenomenological-based models*, exploiting isotropic exponential and power-law functions, have been largely used in the past to characterize the overall mechanical behavior of arteries, although their material parameters are not related to the vessel wall structure and are often difficult to physically interpret. On the contrary, the *structural invariant-based models* are based on the theory of deformation invariants and, in particular, on additional invariants able to capture some structural aspects of the tissue, as the orientation of collagen fibers, the dispersion in the orientation, and the associated anisotropy of the material properties.

In this scenario, the present study wants to investigate the reliability of constitutive models, commonly used to describe the passive mechanical behavior of arteries, comparing the complexity of the respective formulations and their capability to fit human carotid experimental data available in the literature. In particular, we start with the isotropic strain-energy function proposed by Demiray [18] and the one proposed by Harinton [29], already used to characterize the overall mechanical behavior of a human carotid bifurcation [30,31]. Then, we consider the anisotropic strain-energy function with two-fibe families proposed by Holzapfel et al. [24] and the one with four-fiber families proposed by Baek et al. [27]. Finally, in the context of works conceived for modeling fiber distribution, we also consider the models of Holzapfel et al. [25] and Gasser et al. [26].

Once an arterial model is defined, the correct identification of the material parameters involved in its expression represents a fundamental step in constitutive modeling. The process of identification requires experimental data obtained usually from mechanical tests and the solution of an inverse problem using optimization algorithms.In view of the problem at hand, the six investigated strain-energy functions are calibrated with respect to the experimental data reported in the work of Delfino [30] and in the one of Sommer et al. [32]. Both studies [30] and [32] refer to extension/inflation tests, respectively, performed in force-controlled and in stretch-controlled conditions. The intent toward extension/inflation tests comes from the fact that such tests preserve the native geometry of the artery and closely reproduce the in-vivo loading conditions. Hence, following [33], the *overall* arterial mechanical response may be characterized.

Moreover, the two experimental works under investigation provide geometrical and residual data usable to include residual stresses in the arterial model. It should be noted that, several studies [21,34–37] have demonstrated that, at the physiological state, residual stresses reduce the high stress concentration at the inner radius, inducing a stress redistribution through the thickness. It has also been speculated that such a distribution is very close to uniform and increasing with the radius [38]. Hence, the introduction of residual stresses on the arterial model cannot be discarded to get a true stress distribution throughout the arterial wall.In order to incorporate the important features of residual stresses, we follow the so-called *opening angle method* proposed by Choung and Fung [34], accordingly the carotid artery is modeled as a thick-wall cylindrical tube. Although this is a schematization of the arterial geometry, it also ables to take into account the multi-layer structure of the arterial wall [24,39], where each layer (*intima*, *media* and *adventitia*) has different composition and structural organization of the tissue components [15,24,40,41].

Clearly, the performance and the predictive capabilities of a multi-layer model are improved if the model calibrations are performed on experimental data referring to each single layer. To our knowledge, a multi-layer structural model has been proposed in the work of Holzapfel et al. [24] and subsequently used, for example, in Holzapfel et al. [39] and Wang et al. [42], to calibrate experimental data of rabbit carotids and porcine coronaries, respectively.Regarding human data, the work of [32] is the first study which provide extension/inflation data and residual parameters on excised adventitia and media-intima layers of carotid arteries.

In the following, we briefly present the paper organization. Section 2 starts with a short discussion on the kinematics and equilibrium equations related to the extension/inflation test. Then, the constitutive models typically used to describe the mechanical behavior of human arteries is presented. In Sect. 4, we focus on the optimization method used to identify material parameters, whereas the fitting results are presented in Sect. 5 and discussed in Sect. 6. Finally, the conclusions are presented in Sect. 7.

2 Material and Method

To describe the extension/inflation test, the arterial wall is assumed to be a thick-wall cylindrical tube (with one and two-layers structures), subjected to an internal pressure P_i and to an axial force F_z. Assuming axial symmetry of the tube and for such loading conditions, the deformation is torsion-free, so that the cylindrical shape of the tube is preserved and the problem can be described by a cylindrical coordinate system.

To include residual stresses in the arterial model, we follow the so-called *opening angle method*, proposed by Choung and Fung [34]. According to this approach, the reference configuration is represented by a circular open sector defined by a sector angle α, and the residual stress/strain may be defined by two parameters: the axial residual stretch $\lambda_{z_{\text{res}}}$ (released after axial excision) and the sector angle α (measured in the open geometry after a radial cut).

In the following, we summarize the kinematics and the equilibrium equations related to the extension/inflation problem under investigation and then, we present the constitutive models adopted to describe the arterial mechanical behavior.

2.1 Kinematics

Following the *opening angle method*, we define three configurations: (i) the reference configuration Ω_0, which is load-free and stress-free; (ii) the intermediate configuration Ω^*, which is load-free but residually-stressed; and finally (iii) the current configuration Ω, which is loaded by a pressure P_i and an axial force F_z, see Fig. 1.

In the reference configuration Ω_0, the position of a particle is identified by the material point $\mathbf{X}$ with cylindrical coordinates (R, Θ, Z), see Fig. 1a:

$$R_i \leq R \leq R_o, \quad 0 \leq \Theta \leq 2\pi - \alpha, \quad 0 \leq Z \leq L, \tag{1}$$

being R_i and R_o the inner and the outer radius, respectively, and L the length of the open sector.

In the intermediate configuration Ω^*, the same particle is identified by $\mathbf{X}^*$ with cylindrical coordinates (ρ, ϑ, ζ), see Fig. 1b:

$$R_i^* \leq \rho \leq R_o^*, \quad 0 \leq \vartheta \leq \pi, \quad 0 \leq \zeta \leq L^*, \tag{2}$$

being R_i^* and R_o^* the inner and the outer radius, respectively, and L^* the length of the tube expressed as $L^* = \lambda_{z_{\text{res}}} L$ with $\lambda_{z_{\text{res}}}$ the residual axial stretch of the tube with respect to Ω_0.

Finally, in the current configuration Ω, the spatial counterpart of the particle is identified by the point $\mathbf{x}$ with cylindrical coordinates (r, θ, z), see Fig. 1c:

$$r_i \leq r \leq r_o, \quad 0 \leq \theta \leq 2\pi, \quad 0 \leq z \leq l, \tag{3}$$

being r_i and r_o the inner and outer radius, respectively, and l the length of the tube expressed as $L = \lambda_{z_{\text{load}}} L^*$ with $\lambda_{z_{\text{load}}}$ the axial stretch of the tube with respect to Ω^*.

Following [34], the total deformation map associated to the sector closing as well as to the inflation and axial elongation can be described via two successive maps: the first one, $\varphi_1 : \Omega_0 \to \Omega^*$, $\mathbf{X} \mapsto \mathbf{X}^*$, mapping material particles from the reference to the intermediate configuration; and the second one, $\varphi_2 : \Omega^* \to \Omega$, $\mathbf{X}^* \mapsto \mathbf{x}$, mapping the same particles from the intermediate to the current configuration.

If the material is assumed to be incompressible (i.e., the volume of the tube is preserved) the total map, $\varphi : \Omega_0 \to \Omega$, $\mathbf{X} \mapsto \mathbf{x}$, may be described by the equations:

$$r = r(R) = \sqrt{\frac{R^2 - R_i^2}{\kappa \lambda_z} + r_i^2}, \quad \theta = \kappa \Theta, \quad z = \lambda_z Z, \tag{4}$$

with $\kappa = 2\pi / (2\pi - \alpha)$ a measure of the opening angle. Due to the map composition, $\varphi = \varphi_2 \circ \varphi_1$, the total axial stretch λ_z can also be expressed as $\lambda_z = \lambda_{z_{\text{load}}} \lambda_{z_{\text{res}}}$.

In cylindrical coordinates the deformation gradient $\mathbf{F} = \partial \mathbf{x} / \partial \mathbf{X}$ has the following diagonal matrix representation:

$$\mathbf{F} = \text{diag}\left[\lambda_r, \lambda_\theta, \lambda_z\right] = \text{diag}\left[\frac{\partial r}{\partial R}, \frac{r}{R}\frac{\partial \theta}{\partial \Theta}, \frac{\partial z}{\partial Z}\right], \tag{5}$$

with λ_r, λ_θ, λ_z the principal stretches in the radial, circumferential and axial direction, respectively. With positions (4), the principal stretches λ_r, λ_θ, λ_z become:

$$\lambda_r = \frac{R}{\kappa \lambda_z r}, \quad \lambda_\theta = \frac{kr}{R}, \quad \lambda_z = \frac{z}{Z}. \tag{6}$$

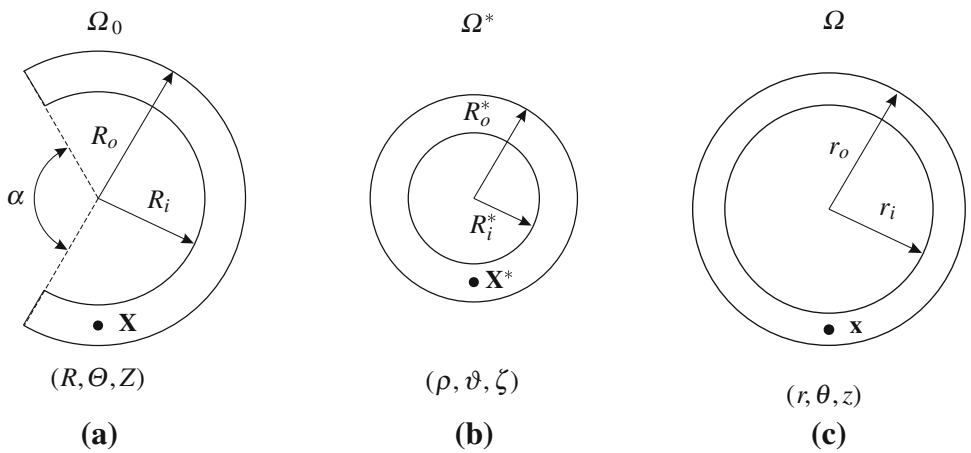

Fig. 1 Geometry of an arterial ring and cylindrical coordinate system in the **a** reference configuration Ω_0, **b** intermediate configuration Ω^*, and **c** current configuration Ω

It is straightforward to verified that the principal stretches in Eq. (6) satisfy the incompressibility condition $J = \det \mathbf{F} = \lambda_r \lambda_\theta \lambda_z = 1$. Finally, the right Cauchy-Green strain tensor $\mathbf{C} = \mathbf{F}^T \mathbf{F}$ takes the diagonal form:

$$\mathbf{C} = \mathrm{diag}\left[\lambda_r^2, \lambda_\theta^2, \lambda_z^2\right] = \mathrm{diag}\left[\left(\frac{\partial r}{\partial R}\right)^2, \left(\frac{r}{R}\frac{\partial \theta}{\partial \Theta}\right)^2, \left(\frac{\partial z}{\partial Z}\right)^2\right]. \tag{7}$$

2.2 Equilibrium and Boundary Conditions

Assuming that all body forces can be neglected, the equilibrium equations in terms of the Cauchy stress tensor $\boldsymbol{\sigma}$ are:

$$\mathrm{div}\boldsymbol{\sigma} = \mathbf{0} \quad \text{and} \quad \boldsymbol{\sigma} = \boldsymbol{\sigma}^T, \tag{8}$$

with $\mathrm{div}(\bullet)$ the spatial divergence operator. In the radial direction, the boundary conditions correspond to a prescribed pressure P_i on the inner radius and to zero pressure on the outer radius:

$$\boldsymbol{\sigma}\mathbf{n} \cdot \mathbf{n} = -P_i \quad \text{at} \quad r = r_i, \quad \boldsymbol{\sigma}\mathbf{n} \cdot \mathbf{n} = 0 \quad \text{at} \quad r = r_o, \tag{9}$$

with $\mathbf{n}$ the unit outward normal to the surface boundary.

Due to the specific problem (extension/inflation of an axial-symmetric tube) wherein the deformation depends only on the radius r, the equilibrium equation (8) reduces to the radial one:

$$\frac{\mathrm{d}\sigma_{rr}}{\mathrm{d}r} + \frac{1}{r}\left(\sigma_{rr} - \sigma_{\theta\theta}\right) = 0, \tag{10}$$

to be solved with boundary conditions: $\sigma_{rr}(r_i) = -P_i$ and $\sigma_{rr}(r_o) = 0$.

Integrating Eq. (10) and using the boundary condition $\sigma_{rr}(r_i) = -P_i$, the radial stresses through the thickness are computed as follows:

$$\sigma_{rr}(\xi) = -P_i + \int_{r_i}^{\xi} \left(\sigma_{\theta\theta} - \sigma_{rr}\right) \frac{\mathrm{d}r}{r}, \tag{11}$$

with ξ ranging between r_i and r_o.Assuming the current radius ξ equal to the outer radius r_o and using the boundary condition $\sigma_{rr}(r_o) = 0$, it follows from Eq. (11) the expression of the internal pressure P_i at the inner surface:

$$P_i = \int_{r_i}^{r_o} \left(\sigma_{\theta\theta} - \sigma_{rr}\right) \frac{\mathrm{d}r}{r}. \tag{12}$$

On the contrary, the axial force F_z is computed by imposing the global equilibrium in the axial direction. Since the terminal parts of the tube are supposed to be closed, the internal pressure P_i also contributes to the equilibrium in the axial direction as follows:

$$F_z + \pi {r_i}^2 P_i = \pi \int_{r_i}^{r_o} 2\sigma_{zz} r \, \mathrm{d}r, \tag{13}$$

which may be rewritten in the form presented in [15,24]:

$$F_z = \pi \int_{r_i}^{r_o} \left(2\sigma_{zz} - \sigma_{\theta\theta} - \sigma_{rr}\right) r \, \mathrm{d}r. \tag{14}$$

Table 1 Investigated *isotropic* strain-energy functions: $W = W_{\mathrm{iso}} - p(I_3 - 1)$

Model	Ref.	W_{iso}
Demiray 1972	[18]	$\frac{a}{2b}\{\exp[b(I_1 - 3)] - 1\}$
Harinton 2007	[29]	$c(I_1 - 3) + \frac{a}{2b}\{\exp[b(I_1 - 3)^2] - 1\}$

2.3 Material Model

In the context of nonlinear hyper-elasticity the passive mechanical behavior of the arterial wall is described in terms of a strain-energy function W per unit reference volume from which the Cauchy stress tensor $\boldsymbol{\sigma}$ is obtained by derivation of W with respect to the strain tensor $\mathbf{C}$ [15,23,43]:

$$J\boldsymbol{\sigma} = -p\mathbf{I} + 2\mathbf{F}\frac{\partial W}{\partial \mathbf{C}}\mathbf{F}^T, \tag{15}$$

with p a Lagrange multiplier accounting for the incompressibility assumption.

Clearly, to have an explicit relationship of the previous mentioned constitutive law, a particular form of the strain-energy function W have to be defined. In this study, we consider the isotropic (exponential) strain-energy function of Demiray [18] and its modification form proposed by Harinton [29]. Then, we review the anisotropic strain-energy function with two-fiber families of Holzapfel et al. [24] and the one with four-fiber families proposed subsequently by Baek et al. [27]. Finally, in the context of works conceived for modeling fiber distribution, we also consider the models of Holzapfel et al. [25] and Gasser et al. [26].

In the following, we briefly explain both the isotropic and anisotropic formulations, with a focus on the notation adopted and the quantities involved in such expressions. Finally, we list the isotropic strain-energy functions in Table 1 and the anisotropic strain-energy functions in Table 2, respectively.

Table 2 Investigated *anisotropic* strain-energy functions: $W = W_{\text{iso}} + W_{\text{aniso}} - p\,(I_3 - 1)$

Model	Ref.	W_{iso}	W_{aniso}
Holzapfel 2000	[24]	$c\,(I_1 - 3)$	$\frac{a}{2b}\sum_{i=1}^{2}\{\exp[b({I_4}^i - 1)^2] - 1\}$
Baek 2007	[27]	$c\,(I_1 - 3)$	$\frac{a}{2b}\sum_{i=1}^{4}\{\exp[b({I_4}^i - 1)^2] - 1\}$
Holzapfel 2005	[25]	$c\,(I_1 - 3)$	$\frac{a}{2b}\sum_{i=1}^{2}\{\exp[b\{(1-\rho)(I_1 - 3)^2 + \rho({I_4}^i - 1)^2\}] - 1\}$
Gasser 2006	[26]	$c\,(I_1 - 3)$	$\frac{a}{2b}\sum_{i=1}^{2}\{\exp[b(\kappa I_1 + (1-3\kappa){I_4}^i - 1)^2] - 1\}$

2.3.1 Isotropic Strain-Energy Functions

For incompressible and isotropic models, the strain-energy function W is written as:

$$W = W_{\text{iso}}\,(I_1) - p\,(I_3 - 1)\,, \tag{16}$$

with I_1 and I_3 the first and the third invariant of the right Cauchy-Green strain tensor $\mathbf{C}$, defined as:

$$I_1 = \text{tr}\mathbf{C} = \lambda_r^2 + \lambda_\theta^2 + \lambda_z^2, \quad I_3 = \det \mathbf{C} = \lambda_r^2\lambda_\theta^2\lambda_z^2. \tag{17}$$

The investigated isotropic strain-energy function of Demiray [18] and of Harinton [29] are defined respectively as:

$$\begin{aligned} W_{\text{iso}} &= \frac{c_1}{2c_2}\{\exp[c_2(I_1 - 3)] - 1\}, \\ W_{\text{iso}} &= c\,(I_1 - 3) + \frac{c_1}{2c_2}\{\exp[c_2(I_1 - 3)^2] - 1\}, \end{aligned} \tag{18}$$

with $c_1 > 0$ a stress-like material parameters, c_2 a dimensionless parameter, and $c > 0$ the stress-like material parameter for the *neo-Hookean* potential.

2.3.2 Anisotropic Strain-Energy Functions

For incompressible and anisotropic models, the strain-energy function W is split into an isotropic part W_{iso}, associated to the elastin matrix, and to an anisotropic part W_{aniso}, associated to the collagen fibers embedded in the matrix. The fiber architecture is introduced through the definition of additional invariants associated to the collagen fibers.

Following [44,45], the strain-energy function W is written as:

$$W = W_{\text{iso}}\,(I_1) + W_{\text{aniso}}\left({I_4}^1, {I_4}^2, \ldots, {I_4}^{N_f}\right) - p\,(I_3 - 1)\,, \tag{19}$$

with N_f the total number of fibers and ${I_4}^i$ the forth invariant associated to the ith fibers family:

$${I_4}^i = \mathbf{C} : \mathbf{a}_0^i \otimes \mathbf{a}_0^i = \lambda_1^2 \cos^2\beta^i + \lambda_2^2 \sin^2\beta^i, \tag{20}$$

with $\mathbf{a}_0^i$ the unit vector denoting the direction of the ith fibers family in the reference configuration, and β^i the angle between $\mathbf{a}_0^i$ and a given direction, usually the circumferential one.

The four investigated anisotropic models have the same isotropic contribution, i.e., the *neo-Hookean* potential $W_{\text{iso}} = c\,(I_1 - 3)$, whereas the anisotropic part W_{aniso}, is modeled by an exponential function whose expression differs from case to case, see Table 2. The simplest expression for W_{aniso} generalized to N_f collagen fibers is given by:

$$W_{\text{aniso}} = \sum_{i=1}^{N_f} \frac{a^i}{2b^i}\{\exp[b^i({I_4}^i - 1)^2] - 1\}, \tag{21}$$

with $a^i > 0$ a stress-like parameter and $b^i > 0$ a dimensionless parameter. The contribution of the ith fibers family is disregarded from the potential when such family is compressed, i.e., when ${I_4}^i < 1$.

In particular, in the *Holzapfel 2000 model* [24] only two-fiber families (i.e., $N_f = 2$) are considered. Such fibers are assumed diagonally arranged (i.e., $\beta_1 = -\beta_2 = \beta$) and mechanically equivalent (i.e., $a^1 = a^2 = a$ and $b^1 = b^2 = b$).

In the *Baek 2007 model* [27] the number of fibers families is incremented to four (i.e., $N_f = 4$). Precisely, two of such fibers families are diagonally arranged and mechanically equivalent as in *Holzapfel 2000 model*, whereas the other two are supposed circumferentially and axially oriented (i.e., $\beta^4 = 0°$ and $\beta^3 = 90°$) with the same mechanical properties (i.e, $a^3 = a^4 = a'$ and $b^3 = b^4 = b'$).

The last two anisotropic strain-energy functions (i.e., the model of Holzapfel et al. [25] and the one of Gasser et al. [26]) improve the previous mentioned *Holzapfel 2000 model* including informations on the fiber distribution.

In the *Holzapfel 2005 model* [25], the anisotropic part W_{aniso} takes the form:

$$W_{\text{aniso}} = \frac{a}{2b}\sum_{i=1,2}\{\exp[b\{(1-\rho)(I_1-3)^2 + \rho({I_4}^i - 1)^2\}] - 1\}, \tag{22}$$

with $\rho \in [0, 1]$ a weighting factor between the full isotropy ($\rho = 0$) and the full fiber alignment ($\rho = 1$), which has not structural correspondences.

On the contrary, in the *Gasser 2006 model* [26], the anisotropic part W_{aniso} is given by:

$$W_{\text{aniso}} = \frac{a}{2b} \sum_{i=1,2} \left\{ \exp\left[b(I_{\langle 4 \rangle}{}^i - 1)^2 \right] - 1 \right\},$$
$$I_{\langle 4 \rangle}{}^i = \mathbf{C} : \left[\kappa \mathbf{I} + (1 - 3\kappa) \mathbf{a}_0^i \otimes \mathbf{a}_0^i \right], \tag{23}$$

with $\kappa \in [0, 1/3]$ the fiber distribution parameter to see in an integral sense [26]. The limits $\kappa = 0$ and $\kappa = 1/3$ correspond to full fiber alignment (no dispersion) and to full isotropy.

It should be noted that in the *Gasser 2006 model* the distribution parameter, κ, derive from a structure tensor approach [46] wherein a *von Mises* function is assumed for modeling fiber splay. On the contrary, in the *Holzapel 2005 model* the distribution parameter, ρ, is only an additional scalar coefficients to weight the dependence on both invariants I_1 and I_4. However, for a detailed comparison of both the models [25] and [26], we suggest the reader to refer to the review work of Holzapfel and Ogden [47].

2.3.3 Model Prediction of Cauchy Stresses and Extension/Inflation Loads

Once the strain-energy function W is given, we can compute the Cauchy stresses in terms of W using Eq. (15). For axial-symmetric deformations and either isotropic or orthotropic materials, the tangential stresses are not present. Hence, the normal stresses become the principal ones. Following [24] and along with the assumption of incompressibility, the expression of the principal stresses σ_{rr}, $\sigma_{\theta\theta}$ and σ_{zz} take the following form:

$$\sigma_{rr} = -p + \lambda_r \frac{\partial W}{\partial \lambda_r}, \qquad \sigma_{\theta\theta} = -p + \lambda_\theta \frac{\partial W}{\partial \lambda_\theta},$$
$$\sigma_{zz} = -p + \lambda_z \frac{\partial W}{\partial \lambda_z}. \tag{24}$$

Substituting Eq. (24) in Eq. (12) and Eq. (14), we can express the internal pressure P_i and the axial force F_z in terms of W, respectively, as follows:

$$P_i = \int_{r_i}^{r_o} \left[\lambda_\theta \frac{\partial W}{\partial \lambda_\theta} - \lambda_r \frac{\partial W}{\partial \lambda_r} \right] \frac{\mathrm{d}r}{r},$$
$$F_z = \pi \int_{r_i}^{r_o} \left[2\lambda_z \frac{\partial W}{\partial \lambda_z} - \lambda_\theta \frac{\partial W}{\partial \lambda_\theta} - \lambda_r \frac{\partial W}{\partial \lambda_r} \right] r \mathrm{d}r. \tag{25}$$

Equation (25) defines the model prediction loads to be used in the optimization procedure.

Subtracting Eq. $(24)_1$ from Eq. $(24)_2$ and from Eq. $(24)_3$, respectively, we can eliminate the Lagrange multiplier p and write the stress differences $\sigma_{\theta\theta} - \sigma_{rr}$ and $\sigma_{zz} - \sigma_{rr}$ as follows:

$$\sigma_{\theta\theta} - \sigma_{rr} = \lambda_\theta \frac{\partial W}{\partial \lambda_\theta} - \lambda_r \frac{\partial W}{\partial \lambda_r}, \quad \sigma_{zz} - \sigma_{rr} = \lambda_z \frac{\partial W}{\partial \lambda_z} - \lambda_r \frac{\partial W}{\partial \lambda_r}. \tag{26}$$

Finally, substituting the current radial stress (11) in Eq. (26), we can obtain the current circumferential and axial stresses to be used to compute the stress distribution through the thickness.

3 Experimental Data

The experimental data of human common carotid arteries reported in the work of Delfino [30] and Sommer et al. [32] are used to calibrate the two isotropic and the four anisotropic strain-energy functions under investigation. Both studies [30] and [32] refer to extension/inflation tests, respectively, performed in force-controlled and in stretch-controlled conditions. For our calibrations, we consider the data on common carotid arteries obtained digitizing the curves plotted in the two works, i.e., in Figs. 4, 5, and 6 of [30] and in Fig. 5 of [32], respectively. For the sake of completeness, the experimental procedures adopted in the works [30] and [32] are summarized in the following.

In the work of Delfino [30], the intact specimens of common carotid artery were loaded by an internal pressure P_i (ranging from 0 to 24 kPa) at three fixed axial stretches λ_z (equal to 1.05, 1.10 and 1.15). The tests were carried out under *force-controlled* conditions, i.e., an axial force F_z (changing with the pressure P_i) was applied to held constant the axial stretch λ_z during the test. After the extension/inflation procedures, the author estimated in the intermediate configuration Ω^* the inner and outer average radii $\rho_i = 3.1$ mm and $\rho_o = 4.0$ mm (corresponding to a measured thickness $\eta = 0.90$ mm). After a radial cut, i.e., in the reference configuration Ω_0, the author measured an inner radius $R_i = 4.46$ mm and an opening angle $\alpha = 100°$. On the contrary, the author assumed the reference thickness H and the residual axial stretch $\lambda_{z_{\text{res}}}$ to be equal to the corresponding values in the intermediate configuration Ω^*, i.e., 0.9 mm and 1, respectively.

In the work of Sommer et al. [32], the intact specimens of common carotid artery were initially pre-stretched (with values of the initial axial stretch ranging from 1.0 to 1.3 in increments of 0.05) and then loaded by an internal pressure P_i (ranging from 0 to 33 kPa). The tests were carried out under *axial stretch-controlled* conditions, i.e., an axial force F_z (corresponding to each initial axial stretch) was applied and held constant during the test. After the extension/inflation procedures, the authors estimated in the intermediate con-

figuration Ω^* the average radii $\rho_i = 2.98$ mm and $\rho_o = 4.15$ mm (corresponding to a thickness $\eta = 1.17$ mm). After a radial cut, i.e., in the reference configuration Ω_0,the author measured an inner radial curvature $\kappa_{R_i} = 0.232\ \text{mm}^{-1}$ (corresponding to $R_i = 4.31$ mm) and an inner axial curvature $\kappa_{Z_i} = -0.110\ \text{mm}^{-1}$.

In the work [32], we have not found a directly expressed measure of the thickness H, of the axial residual stretch $\lambda_{z_{\text{res}}}$ and of the opening angle α for the intact wall of the investigated common carotid arteries. Accordingly, the reference configuration and the residual stresses field are not uniquely identified.In order to overcome this issue, we can precede according to two different approaches. Following [30], we can set the reference thickness H and the residual axial stretch $\lambda_{z_{\text{res}}}$ to be equal to the corresponding values in the intermediate configuration Ω^*, i.e., 1.17 mm and 1, respectively. Then, we can compute the opening angle α imposing that the volume V_0 in the reference configuration Ω_0 is equal to the volume V^* in the intermediate configuration Ω^*. The solution of such equation leads to $\alpha = 81.0°$. Alternatively and in dealing with the idea of no assumptions on H, $\lambda_{z_{\text{res}}}$, and α, the unknown geometrical/residual parameters may be computed together with the material parameters through the optimization procedure. In this work, we adopt the second approach, following the methodology proposed by Stalhand et al. [48,49].

4 Material Parameter Identification

In this section we present the optimization procedure adopted to identify the best-fitting material parameters of a given strain-energy function W with respect to a given experimental data set.

In order to apply the optimization procedure, we define an objective function χ^2 as the sum of squared differences between the experimental measurements and the related model prediction variables.

Focusing on the extension/inflation test, the measured quantities are the internal pressure P_i^{exp} and the axial force F_z^{exp}, where the superscript *exp* stands for experiment. The predicted internal pressure P_i^{mod} and axial force F_z^{mod}, are computed by using Eq. (12) and Eq. (14), respectively, where the superscript *mod* stands for model. Since the experimental tests of Delfino [30] and Sommer et al. [32] were carried out with different protocols (i.e., force-controlled testing and axial stretch-controlled testing, respectively), we consider for each case a different expression of the objective function as explained in the following.

– *Experimental data of Delfino* [30]. In this case, the unknown quantities $\boldsymbol{\kappa}$ are the only material parameters involved in the expression of W. Since the experimental results are presented as pressure and axial force vs. inner radius, the objective function χ^2 is written as the square sum of the residuals of both pressure and axial force:

$$\chi^2(\boldsymbol{\kappa}) = w_P^2 \sum_{a=1}^{N} \left[P_{i,a}^{\text{mod}} - P_{i,a}^{\text{exp}} \right]^2 + w_F^2 \sum_{a=1}^{N} \left[F_{z,a}^{\text{mod}} - F_{z,a}^{\text{exp}} \right]^2, \tag{27}$$

with N the number of data points.Since the experimental values of the axial force are an order of magnitude smaller than those of the pressure, we introduce the weighting factors w_P and w_F to scale properly the two residual terms, so that such terms equally affect the minimization procedure. In this work, w_P and w_F are set to the mean value of experimental pressure and axial force data, respectively.

– *Experimental data of Sommer et al.* [32]. In this case, the unknown quantities $\boldsymbol{\kappa}$ are the material parameters of W as well as the geometrical/residual parameters H, $\lambda_{z_{\text{res}}}$ and α. Since the axial force is held constant during the tests, the experimental results are presented as pressure vs. both the circumferential and axial stretches. It follows that the objective function χ^2 is written as the square sum of the only pressure term:

$$\chi^2(\boldsymbol{\kappa}) = \sum_{a=1}^{N} \left[P_{i,a}^{\text{mod}} - P_{i,a}^{\text{exp}} \right]^2. \tag{28}$$

Clearly, this form does not provide any control on the axial force so that a proper term should be included to penalize the deviation from a constant trend of the axial force. Following [49], the additional term is set equal to the square sum of the difference between consecutive values of the model prediction axial force. Then, the objective function χ^2 takes the following form:

$$\chi^2(\boldsymbol{\kappa}) = \sum_{a=1}^{N} \left[P_{i,a}^{\text{mod}} - P_{i,a}^{\text{exp}} \right]^2 + \varepsilon_F \sum_{a=2}^{N} \left[F_{z,a}^{\text{mod}} - F_{z,a-1}^{\text{mod}} \right]^2, \tag{29}$$

with ε_F a penalty parameter representing a trade-off between an appropriate pressure fitting and the axial force constraints. In our computations, we respect this compromise setting $\varepsilon_F = 0.1$.

Since the geometrical/residual parameters are also computed *via* the optimization procedure, some constraints should be imposed to preserve specific deformation conditions. Following [49,50], we impose an equal constraint to preserve the constant volume to the map between the

reference and the intermediate configuration, Ω^* and Ω_0. Following [32], we relate the axial residual stretch $\lambda_{z_{\text{res}}}$ to the thickness H *via* the equation $\lambda_{z_{\text{res}}} = 1 - \kappa_{Z_i} H$, with the axial curvature κ_{Z_i} measured.

Defined the objective function χ^2 as in (27) or (29), depending on the adopted experimental data, the minimization problem becomes:

$$\begin{cases} \min\limits_{\boldsymbol{\kappa}} \chi^2(\boldsymbol{\kappa}), \\ \text{subjected to:} \quad \boldsymbol{\kappa} \in K, \\ \qquad\qquad\quad V_0 = V^*, \\ \qquad\qquad\quad \lambda_{z_{\text{res}}} = 1 - \kappa_{Z_i} H, \end{cases} \tag{30}$$

with $K = \{\boldsymbol{\kappa}: \ \boldsymbol{\kappa}^- \leq \boldsymbol{\kappa} \leq \boldsymbol{\kappa}^+\}$ the solutions space and $\boldsymbol{\kappa}^-$ and $\boldsymbol{\kappa}^+$ the lower and upper bounds for the material parameters. In our computation, no particular restrictions are imposed on the unknown parameters except those necessary to define the domain of W and discard non-physical/histological solutions. For example, when two-layers structure of the arterial model is considered, we impose box bounds on the orientation angle β to obtain collagen fibers closer to the circumferential direction in the media ($\beta^+ = 45°$) and to the axial direction in the adventitia ($\beta^- = 45\,°$ and $\beta^+ = 90°$) [51,52]. Regarding the geometrical/residual parameters, we set $H^- = 1.17$ mm, $\lambda^-_{z_{\text{res}}} = 1$ and $\alpha^- = 0°$.

The minimization problem (30) has been solved using the *MultiStart solver* available in the Global Optimization Toolbox of Matlab R2011 (The MathWorks, Inc., Natick, MA, U.S.A.), which gives the possibility to use multiple starting values randomly generated within the solution space K. As local solver, we choose the standard function *lsqcurvefit* to solve the no constraint problem and the standard function *fmincon* to solve the constraint problem. Both the functions are available in the Matlab Optimization Toolbox and are based on the *trust-region-reflective method*. The iterations of the considered algorithm can stop when: (i) a maximum number of iterations, $MaxIter$, is performed; (ii) the Newton incremental step becomes smaller than a fixed threshold value, $TolX$; (iii) the infinity norm of the estimated gradient of χ^2 is smaller than a fixed threshold value, $TolFun$. Following [55], in our computations, we also test the sensitivity of the optimal procedure to changes in the values of numerical tolerances $TolX$ and $TolFun$ as well as in the number of starting values. For this purpose, we consider the following numerical setting combinations:

$$\begin{array}{llll} NumSet-1: & TolX=10^{-2} & TolFun=10^{-2} & n=50, \\ NumSet-2: & TolX=10^{-4} & TolFun=10^{-4} & n=50, \\ NumSet-3: & TolX=10^{-2} & TolFun=10^{-2} & n=200. \end{array}$$

Finally, the quality of the optimal solution is validated computing two proper error measures. Following Holzapfel et al. [25], the first adopted error measures is the root mean square error RMSE:

$$RMSE = \sqrt{\frac{\chi^2}{N-q}}, \tag{31}$$

with q the number of parameters and N the number of data points. Following Baek et al. [27], the second error measure is given by:

$$e = \frac{1}{2}\sqrt{\frac{\sum_{a=1}^{N}\left(P_{i,a}^{\text{mod}} - P_{i,a}^{\text{exp}}\right)^2}{\sum_{a=1}^{N}\left(P_{i,a}^{\text{exp}}\right)^2}} + \frac{1}{2}\sqrt{\frac{\sum_{a=1}^{N}\left(F_{z,a}^{\text{mod}} - F_{z,a}^{\text{exp}}\right)^2}{\sum_{a=1}^{N}\left(F_{z,a}^{\text{exp}}\right)^2}}. \tag{32}$$

5 Results

In this section we present the results of the fitting procedure obtained for each considered constitutive model and for each considered set of experimental data. The section is subdivided in two main parts: one related to the data of Delfino [30] and the other one to those of Sommer et al. [32]. Each part is again subdivided in three subsections. The first two subsections summarize the fitting results obtained by using the considered strain-energy functions and assuming the arterial wall to be a one-layer and two-layers thick-wall tube, respectively. In the third subsection, the residual stresses effects on the stress/strain distributions are investigate for both cases.

5.1 Fitting Results on Delfino [30] Data

5.1.1 One-Layer Thick Wall Tube

We start our investigation by considering the one-layer representation of the arterial wall modeled with the isotropic strain-energy functions of Demiray [18] and Harinton [29]; as well as the anisotropic strain-energy functions of Holzapfel et al. [24], Baek et al. [27], Holzapfel et al. [25] and Gasser et al. [26].

Isotropic strain-energy functions

The optimal solutions related to the strain-energy function of Demiray [18] and to the strain-energy functions of Harinton [29] are listed in Table 3. For both cases, the optimization procedure leads to a global minimum and the convergence to the optimal solution is not affect by the different numerical setting. The plots in Fig. 2 show that the experimental data are captured quite well even though the considered strain-energy functions are isotropic and the human carotid tissue is anisotropic. It is worth noting that our results are practically equal to those obtained previously by Delfino [30] and Harinton [29] validating the approach used in this study. The

Table 3 Experimental data of Delfino et al. [30] fitted using isotropic strain-energy functions

W	Material parameters			RMSE	e
	c (kPa)	c_1 (kPa)	c_2 (−)		
Demiray 1972*	–	46.7	15.7	0.0988	0.0802
Harinton 2007**	35.3	309.8	10.3	0.0976	0.0791

* Delfino et al. [30] obtained $c_1 = 44.2$ kPa and $c_2 = 15.7$
** Harinton [29] obtained $c = 36.3$ kPa, $c_1 = 306.5$ kPa and $c_2 = 11.6$

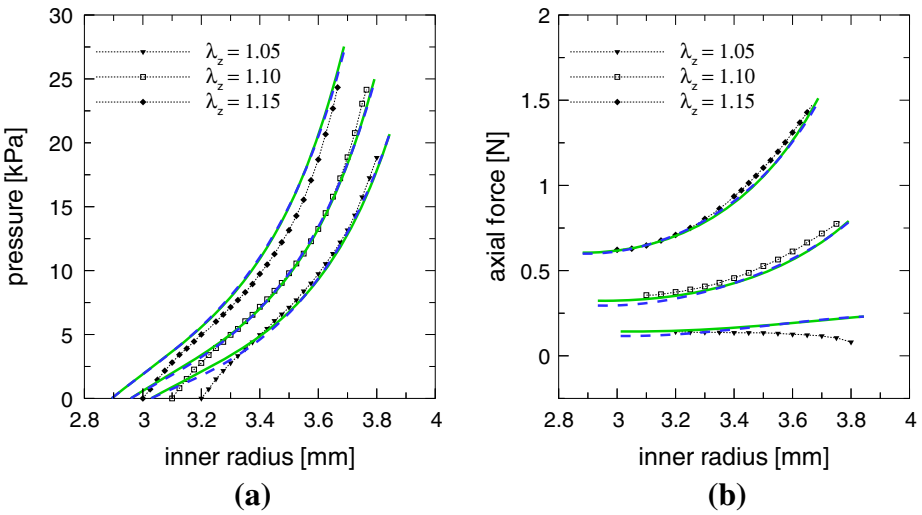

Fig. 2 Experimental data of Delfino [30] (*symbol curves*) fitted using the isotropic strain-energy functions of Demiray [18] (*solid curves*) and of Harinton [29] (*dashed curves*). **a** Plot of pressure vs. inner radius; **b** Plot of axial force vs. inner radius for the three axial stretches $\lambda_z = 1.05$, 1.10 and 1.15

very small difference detected in the values of the material coefficients may be due to the digitization of the curves plotted in [30] and [29].

Anisotropic strain-energy functions

The fitting results have evidenced different fitting capability and different sensitivity to changes in the numerical setting. Consequently, for readability purposes, we list separately the results of each strain-energy function.

– *Holzapfel 2000 model* [24]. For the different numerical setting, the MultiStart solver converges always to the same solution which is regarded as a global rather than a local minimum. The obtained set of material parameters is reported in Table 4. The found angle $\beta = 45.5°$ seems to be reasonable if it is thought as the mean value of the fiber orientations in the media and adventitia layers. In contrast to the results obtained with the isotropic strain-energy functions, the fit quality is worse in all range of pressure as shown in Fig. 3a and confirmed by the higher error measures than the two isotropic cases.
– *Holzapfel 2005 model* [25]. For the different numerical setting, the MultiStart solver converges to the solution reported in Table 4 which may be regarded as a global minimum. Although the predicted curves capture quite well the trend of the data as shown in Fig. 3b and the error measures are lower than the previous mentioned cases, this set of material parameters has not histological correspondences. In fact, for $\beta = 90°$ the optimal solution represents a material with only one family of fibers perfectly aligned to the axial direction. However, the obtained value $\rho = 0$ indicates that the fibers contribution is discarded, reducing the constitutive model to its isotropic form.

Table 4 Experimental data of Delfino et al. [30] fitted using two-fiber anisotropic strain-energy functions

W	N_f	Material parameters					RMSE	e
		c (kPa)	a (kPa)	b (–)	β (°)	ρ/κ (−)		
Holzapfel 2000	2	34.2	10.9	28.3	45.5	–	0.2577	0.1458
Holzapfel 2005	2	15.9	158.3	9.8	90.0	0.000	0.1349	0.0755
Gasser 2006	2	24.9	851.5	179.3	47.3	0.333	0.2098	0.1180

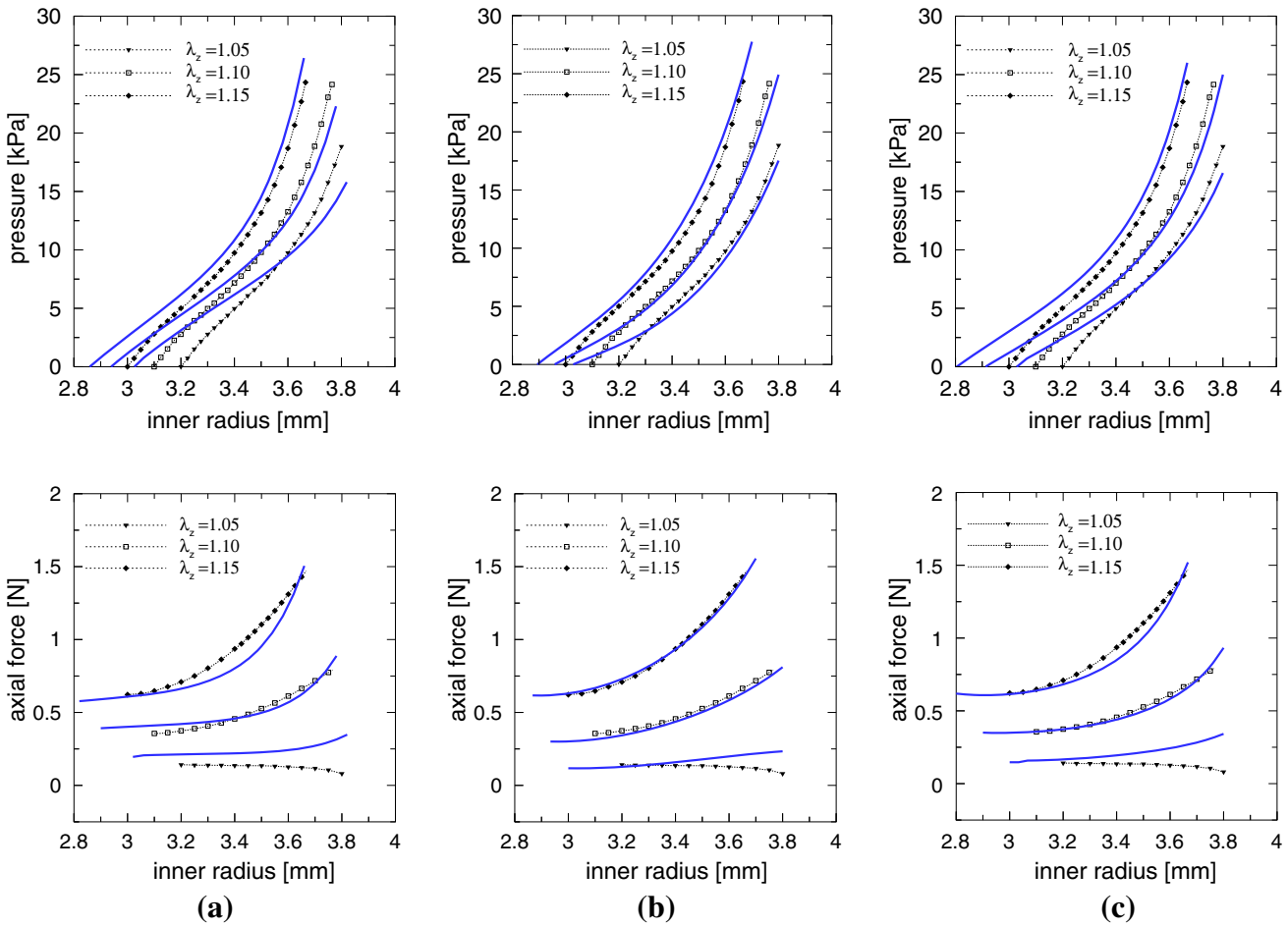

Fig. 3 Experimental data of Delfino [30] (*symbol curves*) fitted using the two-fiber strain-energy functions of: **a** Holzapfel et al. [24]; **b** Holzapfel et al. [25]; and **c** Gasser et al. [26] (*solid curves*). Plots of pressure and axial force vs. inner radius for the three axial stretches $\lambda_z = 1.05$, 1.10 and 1.15

– *Gasser 2006 model* [26]. In contrast to the strain-energy functions mentioned above, the *Gasser 2006 model* proves to be sensitive to changes in the numerical tolerance and the number of starting values. For the *NumSet-1*, the MultiStart solver generates six distinct solutions with decreasing values of the objective function χ^2. The solution with the lowest value of the objective function is reported in Table 4 and the predict responses are plotted in Fig. 3c. Moreover, such solutions correspond to a different fiber architecture. In fact, the first five solutions recover $\kappa = 0.333$ which evidences a full isotropy, whereas the last solution recovers $\kappa = 0.0$ which evidences a full fiber alignment. Repeating the estimation procedure for the other two numerical setting (*NumSet-2*, *NumSet-3*) other multiple local solutions are found.
– *Baek et al. model* [27]. For the different numerical setting, the MultiStart solver converges to the optimal solution reported in Table 5 which may be regarded as a global minimum. Again, we find for the diagonal fibers an orientation angle equal to 45° as in the *Holzapfel 2000 model*.

The error measures in Table 5 as well as the curves plotted in Fig. 4 show that the fit quality improves using four-fiber families rather than two-fiber families.

5.1.2 Two-Layers Thick-Wall Tube

In this section, we consider the arterial wall to be a thick-wall tube with two-layers: the media-intima MI (internal layer) and the adventitia A (outer layer). Since the experimental data of Delfino [30] refer to the intact wall, we assume the media and adventitia layers take up the 2/3 and 1/3 of the wall thickness, respectively [39]. For each layer, we adopt the same expression of the strain-energy function but different sets of material parameters. For lack of experimental data, the simultaneous material parameters identification in both the media and adventitia is performed using the experimental curves of the intact wall.

In contrast to the previous subsection, we reduce the field of our investigations to the only strain-energy function of

Table 5 Experimental data of Delfino et al. [30] fitted using four-fibers anisotropic strain-energy functions

W	N_f	Material parameters						RMSE	e
		c (kPa)	a (kPa)	b (–)	β (°)	$\bar{a}$ (kPa)	$\bar{b}$ (–)		
Baek 2007	4	0.1	39.0	16.1	45.1	23.0	2.7	0.1251	0.0695

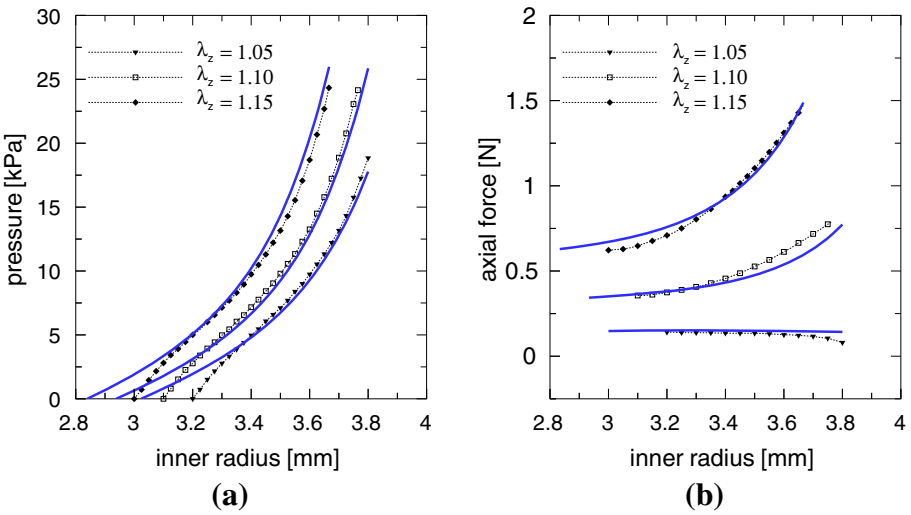

Fig. 4 Experimental data of Delfino [30] fitted using the four-fibers strain-energy fubction of Baek et al. [27]. **a** Plot of pressure vs. inner radius; and **b** plot of axial force vs. inner radius for the three axial stretches $\lambda_z = 1.05$, 1.10 and 1.15

Holzapfel et al. [24]. On one hand, this potential has the lowest number of material parameters, so that we avoid the problems related to the identification of a large number of coefficients. On the other hand, this potential has provided the highest error measures with the one-layer thick-wall tube assumption, so that we want to check the possible improvements on the fitting quality using the two-layers thick-wall tube assumption.

Anisotropic strain-energy functions

– *Holzapfel 2000 model* [24]. For the different numerical setting, the MultiStart solver converges to the solution reported in Table 6. The found values of fibers angle in each layer respect the imposed box bounds. The corresponding mean value is equal to 45°, confirming that the angle $\beta = 45°$ obtained with the one-layer model reflects the overall fibers orientation in the arterial wall. The error measures in Table 6 and the predict responses plotted in Fig. 5 highlight that the fit quality improves the predictive capability of the *Holzapfel 2000 model* using a two-layers rather than one-layer structure.

5.1.3 Stress Distributions Through the Thickness Wall

Using the best-fit material parameters, we compute the stress distributions at $P_i = 13.33$ kPa (physiological state) for the three axial stretches $\lambda_z = 1.05$, $\lambda_z = 1.10$ and $\lambda_z = 1.15$.In order to evidence the effect of residual stresses on the stress distribution, we perform the computations with $\alpha = 0.0°$ (no residual stresses) and $\alpha = 100.0°$ (residual stresses included). Representative examples of stress distributions are plotted for the one-layer thick-wall tube in Fig. 6 and for the two-layer thick-wall tube in Fig. 7. Such examples refer to the axial stretch $\lambda_z = 1.05$.

Although the residual stresses are very low, see Figs. 6c and 7c, their influence on the stress distribution is substantial. In fact, without residual stresses ($\alpha = 0.0°$), the curves are non-linear and monotonically decreasing with the radius. When residual stresses are included ($\alpha = 100.0°$), the high stress concentration at inner radius is reduced. In particular, for the specified value $\alpha = 100.0°$, the curves become linear with similar slopes and monotonically increasing with the radius, i.e., a reversal of the stress trend is evidenced.

For the case with two layers having different material properties, a discontinuity in the values of circumferential and axial stresses takes place at the layer interface. If we compare the stresses in the two layers, we observe that the higher values take place in the media-intima (inner layer) than in the adventitia (outer layer). This occurrence results from the different values of material parameters in each layer.Inside the media-intima, the stress distribution reflects the same trend obtained in the one-layer case which is non-linear monoton-

Table 6 Experimental data of Delfino et al. [30] fitted using the strain-energy function of Holzapfel et al. [24] and with the two-layers assumption

W	Layer	Material parameters				RMSE	e
		c (kPa)	a (kPa)	b (−)	β (°)		
Holzapfel 2000	MI	27.4	20.4	20.0	36.1	0.1572	0.0869
	A	0.01	39.7	19.1	54.7		

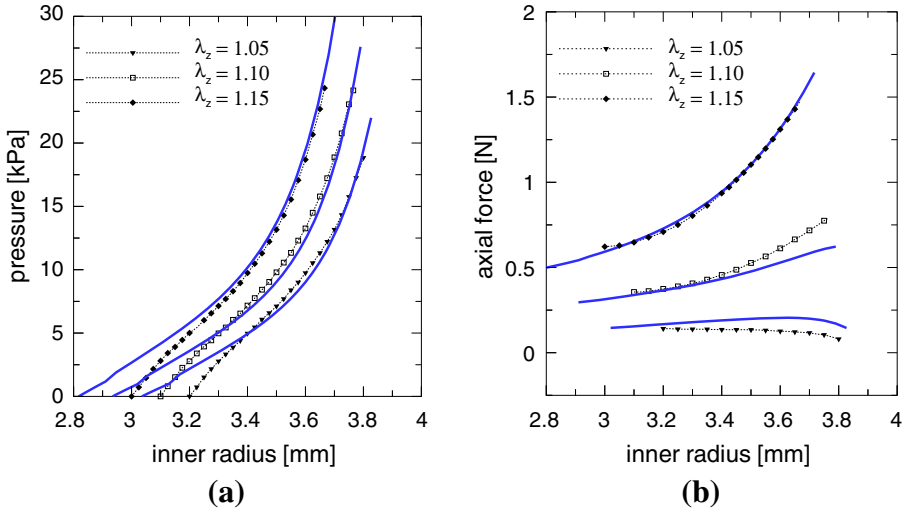

Fig. 5 Experimental data of [30] fitted using the strain-energy function of Holzapfel et al. [24] with the assumption of two-layers thick-wall tube. **a** Plot of pressure vs. inner radius; and **b** plot of axial force vs. inner radius for the three axial stretches $\lambda_z = 1.05$, 1.10 and 1.15, respectively

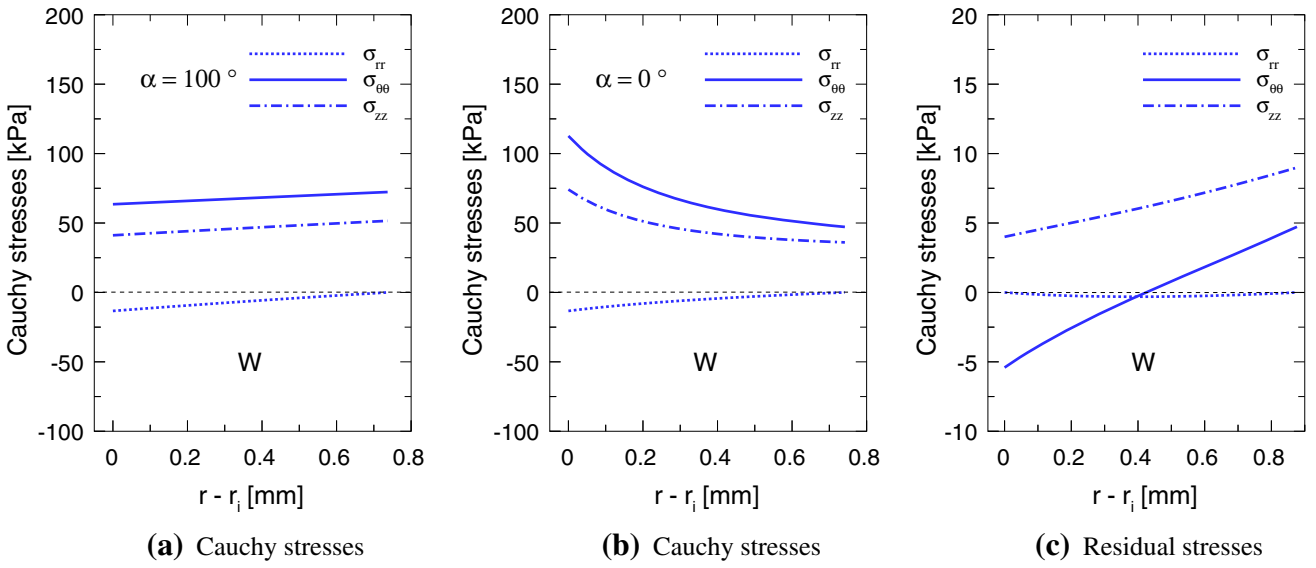

Fig. 6 Cauchy stresses through the wall thickness at $P_i = 13.33$ kPa and $\lambda_z = 1.05$ for **a** $\alpha = 0.0°$ and **b** $\alpha = 100.0°$. **c** Residual stresses. The results are obtained using the strain-energy function of Holzapfel et al. [24] and the one-layer thick-walled tube assumption

ically decreasing for $\alpha = 0.0°$, and linear monotonically increasing for $\alpha = 100.0°$. On the contrary, inside the adventitia the stress profile is closer to be uniform for both cases $\alpha = 0.0°$ and $\alpha = 100.0°$.

Finally, we also investigate how the value of the axial stretch stress affects the stress distribution. In all the considered cases, we have observed that an increment of λ_z induces a shift upwards of σ_{zz} and a shift downwards of $\sigma_{\theta\theta}$ whereas does not affect the radial stresses σ_{rr} (the results are not plotted here).

Figure 8 plots the stretch distributions for both cases $\alpha = 100°$(with residual stresses) and $\alpha = 0°$(without residual stresses), highlighting that at $P_i = 13.33$ kPa the circumferential stretch λ_θ becomes constant through the thickness when residual stresses are included in the arterial model.

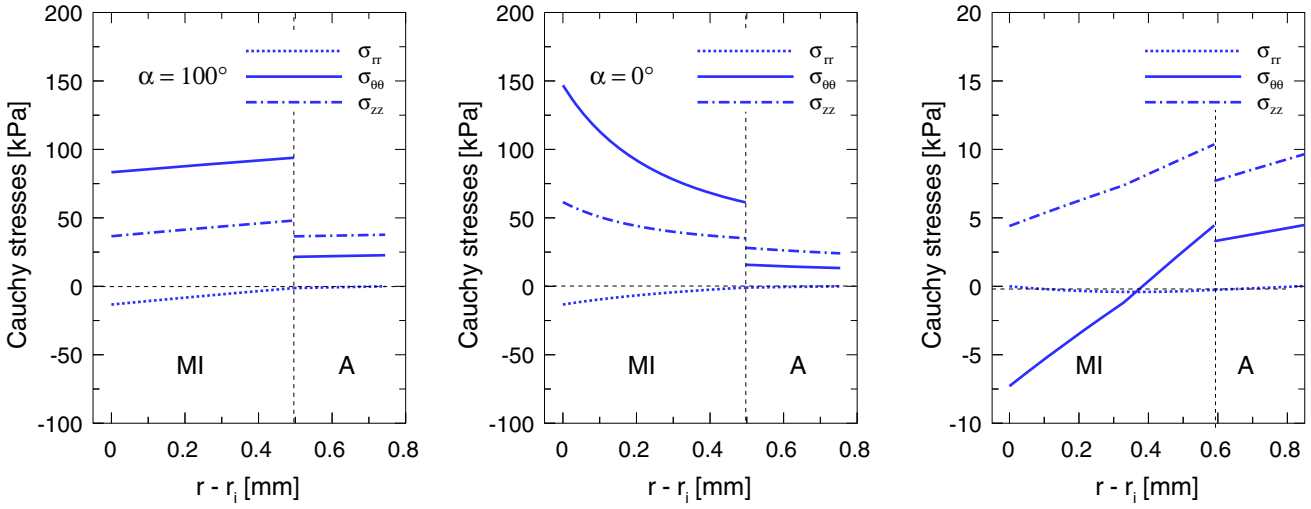

(a) Cauchy stresses **(b)** Cauchy stresses **(c)** Residual stresses

Fig. 7 Cauchy stresses through the wall thickness at $P_i = 13.33$ kPa and $\lambda_z = 1.05$ for **a** $\alpha = 0.0°$ and **b** $\alpha = 100.0°$, respectively. **c** Residual stresses. The results are obtained for the constitutive models of Holzapfel et al. [24] with the two-layers thick-walled tube assumption

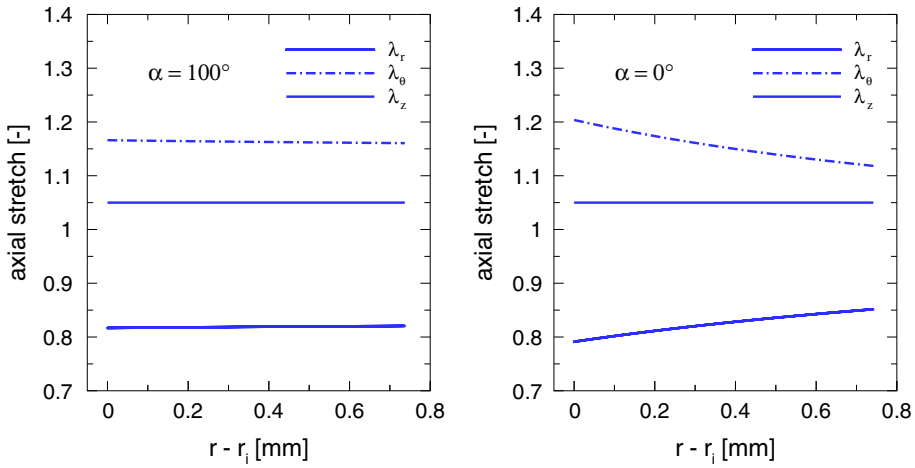

(a) **(b)**

Fig. 8 Radial, circumferential and axial stretches through the thickness at $P_i = 13.33$ kPa and $\lambda_z = 1.05$. The results are obtained for the constitutive models of Holzapfel et al. [24]

5.2 Fitting Results on Sommer et al. [32] Data

Similarly to the previous section, here, we investigate the fitting capability of the considered strain-energy functions with respect to the experimental data of Sommer et al. [32], distinguishing again the case of one-layer and two-layers thick-wall tube.

5.2.1 One-Layer Thick Wall Tube

With respect to the one-layer thick walled tube assumption, the arterial tissue is modeled using (i) the isotropic strain-energy functions of Demiray [18] and Harinton [29]; and (ii) the anisotropic strain-energy functions of Holzapfel et al. [24], Holzapfel et al. [25], Gasser et al. [26] and Baek et al. [27]. In contrast to the results obtained in the previous section, the isotropic strain-energy functions are not able to fit the experimental data of Sommer et al. [32] so that such results are not reported here, but only the ones corresponding the considered anisotropic strain-energy functions.

Anisotropic strain-energy functions

– The anisotropic *Holzapfel 2000 model* [24] and *Holzapfel 2005 model* [25] have evidenced no sensitivity to changes in the numerical setting. The fitting results summarized in Table 7 highlight that the two solutions correspond to the same fibers organization and mechanical behavior. In fact, the obtained value $\rho = 0.97$ indicates fibers strongly aligned to the main direction, i.e., the *Holzapfel 2005 model* reduces to the *Holzapfel 2000 model*. It should be

Table 7 Experimental data of Sommer et al. [32] fitted using the two-fiber anisotropic strain-energy functions

W	N_f	Material and geometrical/residual parameters								RMSE	e
		c (kPa)	a (kPa)	b (−)	β (°)	ρ (−)*	H (mm)	$\lambda_{z_{\text{res}}}$(−)	α (°)		
Holzapfel 2000	2	26.5	20.9	56.5	24.9	–	1.17	1.06	80.9	1.1578	0.0332
Holzapfel 2005**	2	26.6	20.9	56.5	24.9	0.97	1.17	1.06	80.9	1.1982	0.0332
Gasser 2006	2	27.9	28.6	53.3	24.8	0.03	1.17	1.06	80.9	1.1599	0.0321

*κ (−) for the *Gasser 2006* model
** Sommer [32] obtained $c = 27.4$ kPa, $a = 13.0$ kPa, $b = 91.5$, $\beta = 26.1°$ and $\rho = 0.9$

noted that the obtained material parameters are similar to those found by Sommer and Holzapfel [53] validating the approach used in this study. The differences detected, especially for the coefficients a and b, may be due to the digitization of the curves plotted in [32] and to the computations of the reference configuration *via* the optimization procedure. The model predicted curves (pressure vs. stretches) are plotted in Fig. 9 for the four different value of axial force identified by the corresponding axial prestretch $\lambda_z = 1.00, 1.05, 1.10$ and 1.15. The experimental data are captured well at the high pressures, whereas it is not the same at the low pressure values wherein a right shift takes place.

– *Gasser 2006 model* [26]. In contrast to the two strain-energy functions mentioned above, the *Gasser 2006 model* proves to be sensitive to the numerical tolerance and to the number of starting values. For the *NumSet-1*, the MultiStart solver generates nine distinct solutions with decreasing value of the objective function χ^2. Repeating the estimation procedure for the other two numerical setting (*NumSet-2*, *NumSet-3*) other multiple local solutions are found. The solution with the lowest value of the objective function is reported in Table 7 and the corresponding predict responses are plotted in Fig. 9. It should be noted that the multiple solutions correspond to different fiber architectures. In fact, the first solution provides a value of κ near to zero (full fibers alignment). Such value increases progressively for the other solutions until to reach $\kappa = 0.333$ (full isotropy). The results are not presented here. Finally, we also note that the first solution is in agreement with those obtained with the *Holzapfel 2000 model* and the *Holzapfel 2005 model*.
– *Baeck 2007 model* [27]. For the different numerical setting the MultiStart solver converges always to the same solution reported in Table 8, which may be regarded as a global minimum. A closer inspection of the table highlights that the stress-like parameter a' (related to the circumferential and axial fibers) is equal to zero, i.e., the contribution to the mechanical behavior of such fibers is disregarded and the *Baek 2007 model* reduces to the *Holzapfel 2000 model*.

Relatively to the geometrical/residual parameters, we note that the same values of H, $\lambda_{z_{\text{res}}}$ and α are recovered by each model, and that such values are equal to those obtained bypassing the fitting procedure as previously mentioned in Sect. 3.

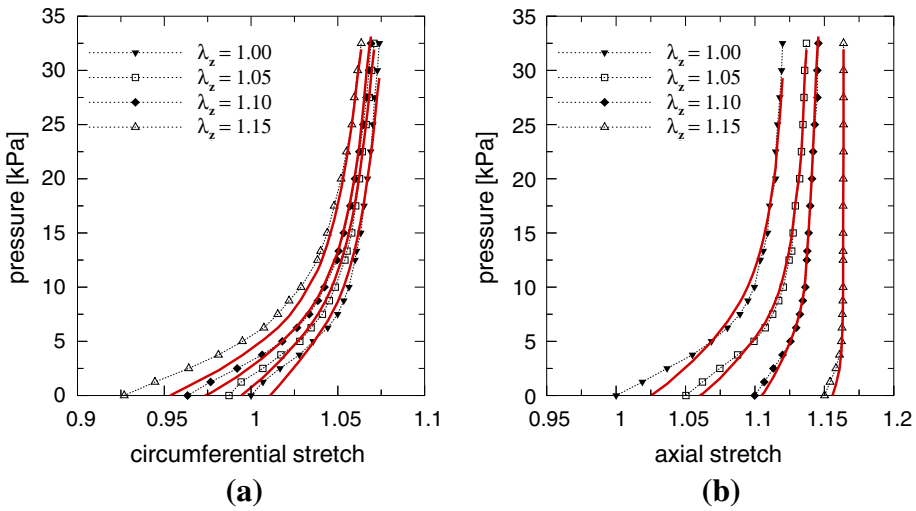

Fig. 9 Experimental data of Sommer et al. [32] fitted using the strain-energy function of Holzapfel et al. [24] with the assumption of one-layer thick-wall tube. **a** Plot of pressure vs. circumferential stretch; and **b** plot of pressure vs. axial stretch

Table 8 Experimental data of Sommer et al. [32] fitted using the four-fibers anisotropic strain-energy function

W	N_f	Material and geometrical/residual parameters									RMSE	e
		c (kPa)	a (kPa)	b (−)	β (°)	a' (kPa)	b' (−)	H (mm)	$\lambda_{z_{\text{res}}}$(−)	α (°)		
Baek 2007	4	26.5	20.0	55.5	25.4	0.00	4.6	1.17	1.06	80.6	1.2075	0.0332

5.2.2 Two-Layers Thick Wall Tube

In this section, we consider the arterial wall to be a thick-wall tube with two-layers: the media-intima MI (internal layer) and the adventitia A (outer layer). As reported in [32], we set the thickness for the media and the adventitia layer to 0.70 mm and 0.47 mm, respectively, and we assume $\lambda_{z_{\text{res}}} = 1.06$ and $\alpha = 80.9°$ as computed in the previous section. It follows that the only material parameters are computed through the optimization procedure.

For each layer, we adopt the same expression of the strain-energy function but different sets of material parameters. Although [32] provides experimental data for the media-intima and adventitia, we identify the two set of material parameters using the experimental curves of the only intact wall as done for the [30] data. Again, although [32] also provides residual data for each layer, we assume the same opening angle and the same axial pre-stretch in the the media-intima and adventitia. Finally, as done for the Delfino [30] data, we reduce the field of our investigations to the only strain-energy function of Holzapfel et al. [24].

Anisotropic strain-energy functions

– *Holzapfel 2000 model* [24].
The optimal solution is reported in Table 9 whereas the model prediction responses are plotted in Fig. 10. Although the optimization procedure is performed using only the data of the intact wall, the predictive capability of the *Holzapfel 2000 model* improves using two-layers rather than one, as evidenced quantitatively by the error measures and qualitatively by the model prediction curves. In fact, in contrast to the one-layer case, the experimental curves are captured well in all range of pressures using a two-layers strtucture.

5.2.3 Stress Distributions Through the Thickness Wall

Using the best-fit material parameters, we compute the stress distributions at $P_i = 13.33$ kPa (physiological state) for the axial forces corresponding to the four axial pre-stretches $\lambda_z = 1.0$, 1.05, 1.10 and 1.15. In order to evidence the effect of residual stresses on the stress distribution, we perform the computations with $\alpha = 0.0°$ (no residual stresses) and $\alpha = 80.0°$ (residual stresses included). Representative examples of stress distributions are plotted for the one-layer thick-wall tube in Fig. 11 and for the two-layer thick-wall tube in Fig. 12. Such examples refer to the force corresponding to the axial pre-stretch $\lambda_z = 1.05$.

As for the Delfino [30] data, we assist to a reduction of the higher stresses manifested at the inner radius in absence of residual stresses. On the contrary, although a flattening of such stresses occurs, we do not assist to a reversal of the circumferential and axial stress distribution for the opening angle $\alpha = 80.9°$.

For the case with two layers, a discontinuity in the values of circumferential and axial takes place at the layer interface.

If we compare the stresses in the two layers, we observe higher values in the adventitia (outer layer) than in the media-intima (inner layer), with exception the circumferential stresses at the inner radius zone for $\alpha = 0°$, see Fig. 12a and b.

6 Discussion

In the present study, we investigate how the complexity of a constitutive model can affect and/or improve the capability to fit human carotid experimental data.

On one hand, regarding constitutive modeling, we consider the two isotropic strain-energy functions proposed

Table 9 Experimental data of sommer et al. [32] fitted using the strain-energy function of Holzapfel et al. [24] and with the two-layers assumption

W	Layer	Material parameters				RMSE	e
		c (kPa)	a (kPa)	b (–)	β (°)		
Holzapfel 2000	MI	0.6	24.8	61.4	4.5	0.5326	0.0154
	A	64.6	14.8	44.4	47.4		

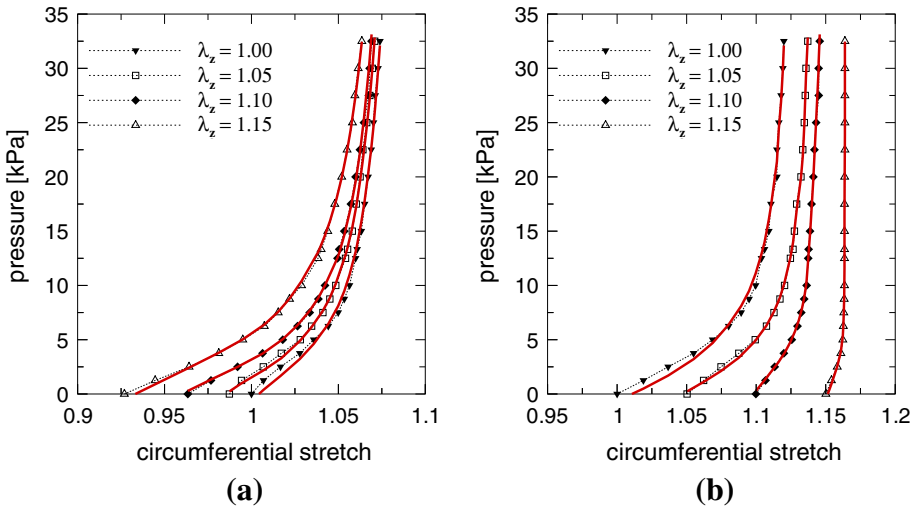

Fig. 10 Experimental data of Sommer et al. [32] fitted using the strain-energy function of Holzapfel et al. [24] with the assumption of two-layers thick-wall tube. **a** Plot of pressure vs. inner radius; and **b** plot of axial force vs. inner radius for the three axial stretches $\lambda_z = 1.05$, 1.10 and 1.15, respectively

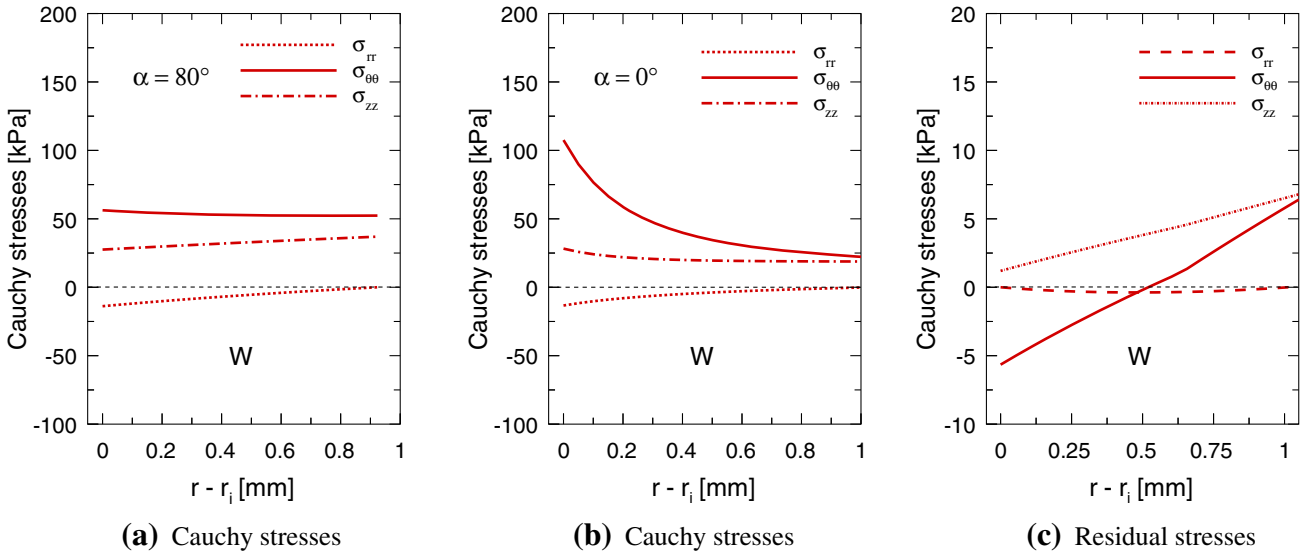

Fig. 11 Cauchy stresses through the wall thickness at $P_i = 13.33$ kPa for the axial pre-stretches $\lambda_z = 1.05$ and for: **a** $\alpha = 80°$, and **b** $\alpha = 0°$. **c** Residual stresses. The results are obtained using the strain-energy funxtion of Holzapfel et al. [24] and the one-layer thick-walled tube assumption

by Demiray [18] and Harinton [29] as well as the four anisotropic strain-energy functions proposed, respectively, by Holzapfel et al. [24], Baek et al. [27], Holzapfel et al. [25] and Gasser et al. [26] for which the only structural tissue information is the collagen fibers architecture. On the other hand, regarding the experimental data, we consider the extension/inflation results reported on both experimental works of Delfino [30] and Sommer [54]. The intent toward extension/inflation tests comes from the fact that such tests preserve the native geometry of the artery and close reproduce the in-vivo loading conditions. In our investigations, we also assume the arterial wall as a thick-wall cylindrical tube to incorporate the important features of multi-layer structure and residual stresses and then, to evaluate their effects on the predicted mechanical response and on the stress distribution through the thickness.

The good quality of the found optimal solutions is validated quantitatively computing proper error measures [25,27] and comparing the related model prediction curves. Following [55], any sensitivity of the optimal solution to changes in the values of tolerance, number of start values and number of iterations is also evaluated.

In the following, we briefly discuss the results obtained from the fitting procedure performed for each considered model and with respect to both the data of Delfino [30] and of Sommer [54]. Subsequently, we present some notes on the research of local and global minima through the MultiStart solver with a focus on the models for which more local minima occur. Then, we discuss the substantial dependence of the stress distribution through the thickness on the residual stresses and on the multi-layer structure of the arterial wall. Finally, we evidence some limitations of the present study.

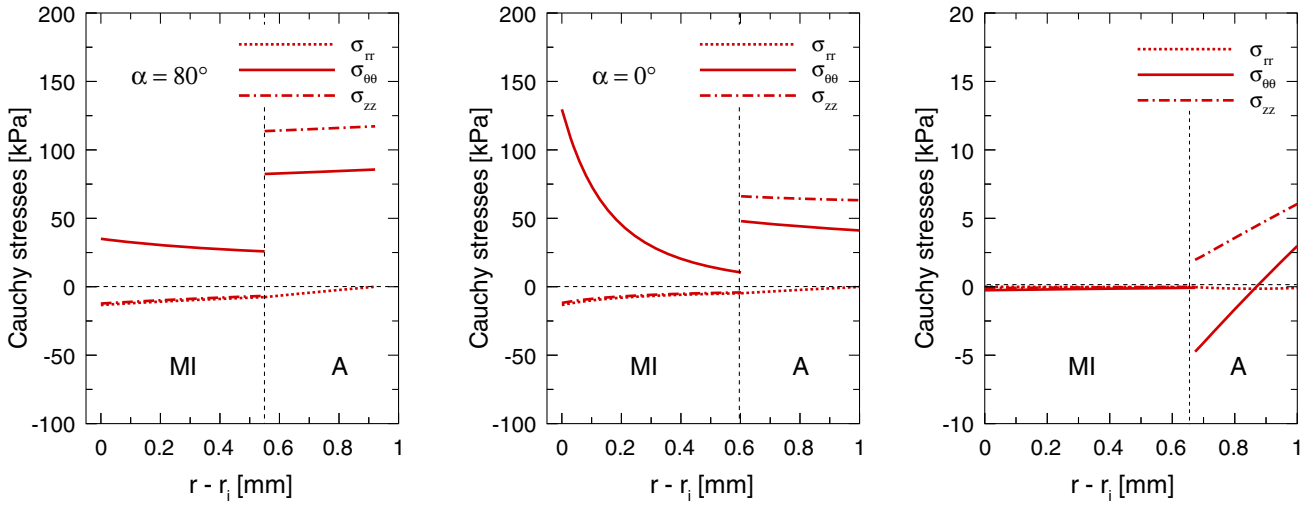

(a) Cauchy stresses **(b)** Cauchy stresses **(c)** Residual stresses

Fig. 12 Cauchy stresses through the wall thickness at $P_i = 13.33$ kPa for the axial pre-stretches $\lambda_z = 1.05$ and for: **a** $\alpha = 80°$ and **b** $\alpha = 0°$, respectively. **c** Residual stresses. The results are obtained using the strain-energy function of Holzapfel et al. [24] and the two-layer thick-walled tube assumption

– *Fitting results on the experimental data of Delfino* [30]
Relatively to the experimental data of Delfino [30], the two isotropic strain-energy functions in conjuction with the one-layer structure assumption provide a good agreement with the experimental data although such data correspond to a typical anisotropic tissue. On the contrary, with our surprise, the *Holzapfel 2000 model* [24] with two-fiber families produces a poor fit. On the other hand, the fitting quality slightly improves using the *Holzapfel 2005 model* [25] and the *Gasser 2006 model* [26], which include a fiber distribution parameter. However, such an improvement is due to the fact that the two models reduce through the optimization procedure to theirs respective isotropic forms.
In other words, although it is well-known that the carotid tissue is anisotropic, it seems that the data of Delfino [30] on intact human carotids highlights an overall mechanical response of isotropic type.From the fitting point of view, such a result could be acceptable although not justified by histological and mechanical evidences. Accordingly, we argue that the assumptions of one-layer thick-wall tube and two-fiber families (with or without dispersion) are not sufficient to provide reasonable solutions for these specific experimental data.
On the contrary, using a one-layer thick-wall tube reinforced by four-fiber families as well as a two-layers thick-wall tube reinforced by two-fiber families, the error measures decrease and the trend of the data is captured quite well considering. In particular, the model with one-layer and four-fiber families achieves lower errors than the model with two-layers and two-fibers. Such a difference can be attributed to the greater number of material parameters for the model with two-layers and to the fact that the experimental data of Delfino [30] refer only to the intact carotid wall, and thus could not be exhaustive for the two-layers wall assumption.
Finally, we recall that all calibrations executed with the one-layer assumption have provided (for the diagonally orientated fibers) an angle β close to 45°, indicating an overall symmetrical fibers arrangement with respect to both the circumferential and longitudinal directions.Such a result is confirmed by the one obtained with the two-layers assumption. In fact, the mean value between the media and adventitia fiber angles is very close to 45°.
– *Fitting results on the experimental data of Sommer et al.* [32]
Relatively to the experimental data of Sommer et al. [32], the two isotropic strain-energy functions are not able to provide reasonable fit to data and then to characterize the overall carotid mechanical behavior. On the contrary, the four investigated anisotropic strain-energy functions capture quite well the considered extension/inflation data, providing the same optimal solution as well as the same good fit to the data.
However, our computations evidence a different predictive capability of the *Holzapfel 2005 model* [25] and *Gasser 2006 model* [26]). In fact, when the fiber distribution is very low (i.e., for $\rho \approx 0.97$ and $\kappa \approx 0.03$, respectively, as occur for the data of Sommer et al. [32]), such models provide a reliable optimal solution.On the contrary, when the fiber distribution is very high (i.e., for $\rho \approx 0$ and $\kappa \approx 1/3$, respectively, as occur for the data of Delfino [30]), the optimal solutions have no histological correspondences. It should be noted that such

results are in agreement with the range of angular distributions suggested recently by Cortes et al. [56], according to which the mechanical behavior of an anisotropic tissue with high fibers dispersion is not captured well by models incorporating such a dispersion with structural approaches.

Finally, we recall that for the data of Sommer et al. [32], the optimization procedures is applied to both material parameters and to some geometrical/residual data (i.e., the reference thickness H, the axial residual stretch $\lambda_{z_{\text{res}}}$ and the opening angle α). Proper box-bounds and equal constraints are used in the minimization in order to avoid non-physical/histological solutions, to preserve specific deformation conditions (such as constant volume, constant axial force) and to prescribe a specific relationship for the axial residual stretch.

– *Local and global minima*

For both experimental data of Delfino [30] and Sommer et al. [32], all constitutive models (with the only exception for the *Gasser 2006 model* [26]) converges to a single optimal solution and such convergence is not affect by the levels of accuracy required by the optimization procedure (i.e., tolerances, maximum number of start values and number of iterations). This result evidences that for such models the optimal set of material parameters represents a global minimum for the corresponding objective function.On the contrary, the *Gasser 2006 model* [26] provides more local solutions whose number and values change with the levels of accuracy required by the optimization procedure. In addition, such local minima correspond to different fibers architecture (i.e., full fiber dispersion and full fiber alignment).

– *Stress distributions through the thickness wall*

For both experimental data of Delfino [30] and Sommer et al. [32], our results confirm the positive effects of the residual stresses on the distribution of circumferential and axial stresses through the thickness [21,34,38]. In fact, residual stresses reduce the high stresses concentration at the inner radius and induce an almost uniform distribution takes place across the wall.

In absence of residual stresses, such a distribution is non-linear and monotonically decreasing with the radius. With residual stresses included, the stress distribution become linear and can also be monotonically increasing. We have also observed that such reversal in the trend of the stress distribution depends on the value of the opening angle α.In fact, we obtain a flattening of the stress distribution for both the opening angle $\alpha = 100°$ (for Delfino [30] data) and $\alpha = 80°$ (for Sommer [54] data), but a change in the trend is manifested only for $\alpha = 100°$. The important role of the opening angle on the stress distribution has been discussed recently in the work of Wang et al. [57], wherein the authors specify that a reversal of the stress distribution can occur (at the physiological state) for values of α higher than 90°.

Finally, we also evidence the dependence of the stress distribution on any material inhomogeneity through the thickness. In fact, a multi-layer structure changes the assessment of the stresses in each layer and induces a discontinuity at the layer interface with a stress jump depending on the values of the material parameters of each adjacent layer. In particular, we obtain stresses are higher in the media-intima layer (inner layer) than in the adventitia (outer layer) for the data of Delfino [30], whereas an opposite result occurs for the data of Sommer [54].

– *Limitations*

In the following, we evidence some limitations of the present study related to the considered constitutive models as well as to the assumptions on the geometrical/residual arterial model.

On one hand, with respect to constitutive models, we have considered *isotropic phenomenologically models* as well as *structural-based models* for which the collagen fiber architecture is the only structural tissue information. Regarding the structural-based models, collagen fibers are assumed embedded in an isotropic non-collageneous matrix and treated as a discrete number of independent units or as continuum distributed units. In view of improving the description of the arterial wall mechanics, *microstructural-based models* which incorporate, for example, fiber-fiber interaction, fiber crimp could be considered [58,59].

On the other hand, with respect to residual stresses, we have assumed the same residual parameters (i.e., the opening angle and the axial residual stretch) for the media-intima and adventitia layers. In actual fact, it is known that residual stresses are still present in such layers after a single cut. In the context of human carotid arteries, such occurrence has been evidenced in the experimental work of Sommer et al. [32]. Hence, for a more realistic arterial modeling, different residual parameters (measured histologically) should be used for the two layers. A step forward in this direction has been made in the recent constitutive modeling work of Sommer et al. [53]. With respect to the multi-layer structure, we have simultaneously calibrated the set of material parameters of each arterial layer, using the experimental data of the intact wall. Clearly, more realistic capabilities of the multi-layer model could be obtained using experimental data of the intact wall in conjunction with the ones of each layer.

7 Conclusions

The ability to describe the mechanical response of human carotid arteries is a crucial topic in the constitutive model-

ing, which is a very active field of research continuously increasing in the biomechanics area.

On one hand, the model should be able to give a good fit over the range of experimental data as well as to provide a realistic stress distribution in the arterial wall. Hence, models taking into account histological, residual and mechanical evidences on the human arterial wall are expected. On the other hand, such models should ensure the uniquely of the optimal set of material parameters *via* the optimization procedure.

In the present study, we have evidenced how the complexity of a constitutive model can affect and/ or improve the capability to fit experimental data of human carotid arteries as well as how the optimal set of material parameters can also depend on the levels of accuracy in the optimization procedure in some cases.

The investigated *isotropic phenomenological* models have evidenced a good capability to characterize the mechanical behavior of arteries only if the overall response is of isotropic type. On the contrary, the investigated *structural invariant-based* model with two-fiber families (perfectly aligned) in conjunction with a one-layer thick-walled tube are not able to capture such a behavior.Again, the *structural invariant-based* models including fiber distribution have evidenced a low capability to characterize the mechanical behavior of tissues with high fibers dispersion.Such unpleasant occurrences are avoided using models with a more number of fibers and more arterial layers. Finally, the inclusion of residual stresses as well as the multi-layer organization on the arterial model cannot be discarded to get a true stress distribution throughout the arterial wall. Such informations could be important to predict the onset and the progression of atherosclerotic lesions, the rupture of aneurysms as well as the stress distribution across the wall under angioplasty and stenting.

In conclusion, we hope that the present paper may be for the readers a critical review of the considered arterial models and a useful guideline for improving understanding of typical problems occuring in fitting experimental data.

Acknowledgments The support of the Cariplo Foundation through the Project Number n.2009.2822 and the PRIN project n. are gratefully acknowledged.

References

1. Casscells W, Naghavi M, Willerson JT (2003) Vulnerable atherosclerotic plaque: a multifocal disease. Circulation 107:2072–2075
2. Chaturvedi S, Bruno A, Feasby T, Holloway R, Benavente O, Cohen S, Cote R, Hess D, Saver J, Spence J, Stern B, Wilterdink J (2005) Carotid endarterectomy—an evidence-based review: report of the therapeutics and technology assessment subcommittee of the american academy of neurology. Neurology 65:794–801
3. Petersen SPV, Rayner M, Leal J, Luengo-Fernandez R, Gray A (2005) European cardiovascular disease statistics. British Heart Foundation (BHF), London
4. Cheng GC, Loree HM, Kamm RD, Fishbein MC, Lee RT (1993) Distribution of circumferential stress in ruptured and stable atherosclerotic lesions: a structural analysis with histopathological correlation. Circulation 87:1179–1187
5. Li Z, Howarth S, Trivedi R, U-King-Im J, Graves M, Brown A, Wang L, Gillard J (2006) Stress analysis of carotid plaque rupture based on in vivo high resolution mri. J Biomech 39:26112622
6. Kiousis DE, Gasser TC (2007) A numerical model to study the interaction of vascular stents with human atherosclerotic lesions. Ann Biomed Eng 35:1857–1869
7. Raghavan ML, Vorp DA, Federle MP, Makaroun MS, Webster MW (2000) Wall stress distribution on three dimensionally reconstructed models of human abdominal aortic aneurysm. J Vasc Surg 31:760769
8. Rodríguez J, Ruiz C, Doblar G, Holzapfel M (2008) Mechanical stresses in abdominal aortic aneurysms: influence of diameter asymmetry and material anisotropy. J Biomech Eng 130:110
9. Gupta BS, Kasyanov VA (1997) Biomechanics of human common carotid artery and design of novel hybrid textile compliant vascular grafts. J Biomed Mater Res 34:341–349
10. Lally C, Dolanb F, Prendergast PJ (2005) Cardiovascular stent design and vessel stresses: a finite element analysis. J Biomech 38:1574–1581
11. Wu W, Qi M, Liu XP, Yang DZ, Wang WQ (2007) Delivery and release of nitinol stent in carotid artery and their interactions: a finite element analysis. J Biomech 40:3034–3040
12. Gasser TC, Holzapfel GA (2007) Modeling plaque fissuring and dissection during balloon angioplasty intervention. Ann Biomed Eng 35:711–723
13. Mortier P, Holzapfel GA, De Beule M, Van Loo D, Taeymans Y, Segers P, Verdonck P, Verhegghe B (2010) A novel simulation strategy for stent insertion and deployment in curved coronary bifurcations: comparison of three drug-eluting stents. Ann Biomed Eng 38:88–99
14. Auricchio F, Conti M, De Beuleb M, De Santisb G, Verheggheb B, Carotid artery stenting simulation:from patient-specific images to finite element analysis. Med Eng Phys. doi:10.1016/j.medengphy.2010.10.011
15. Humphrey JD (2002) Cardiovascular solid mechanics. Cells, tissue and organs. Springer Verlag, New York
16. Spencer AJM (1982) Deformation of fiber-reinforced materials. Oxford University Press, Oxford
17. Spencer AJM (1984) Continuum theory of the mechanics of fibre-reinforced composites. Springer-Verlag, New York
18. Demiray H (1972) A note on the elasticity of soft biological tissues. J Biomech 5:309–311
19. Fung YC, Fronek K, Patitucci P (1979) Pseudoelasticity of arteries and the choice of its mathematical expression. Am J Physiol 237:H620–H631
20. Chuong CJ, Fung YC (1983) Three-dimensional stress distribution in arteries. J Biomech Eng 105:268–274
21. Takamizawa K, Hayashi K (1987) Strain energy density function and uniform strain hypothesis for arterial mechanics. Biophys J 20:7–17
22. Fung YC (1993) Biomechanics: mechanical properties of living tissues. Springer Verlag, New York
23. Ogden RW (1997) Non-linear elastic deformation. Dover, New York
24. Holzapfel GA, Gasser TC, Ogden RW (2000) A new constitutive framework for arterial wall mechanics and a comparative study of material models. J Elast 61:1–48
25. Holzapfel GA, Sommer G, Gasser CT, Regitnig P (2005) Determination of layer-specific mechanical properties of human coronary arteries with nonatherosclerotic intimal thickening and related constitutive modeling. Am J Physiol 289:H2048–H2058

26. Gasser TC, Ogden RW, Holzapfel GA (2006) Hyperelastic modelling of arterial layers with distributed collagen fibre orientations. J R Soc Interface 3:15–35
27. Baek S, Gleason RL, Rajagopal KR, Humphrey JD (2007) Theory of small on large: potential utility in computations of fluid solid interactions in arteries. Comput Method Appl Mech Eng 196:3070–3078
28. Pandolfi A, Vasta M (2012) Fiber distributed hyperelastic modeling of biological tissues. Mech Mater 44:151–162; 3070–3078
29. Hariton I (2007) Vascular biomechanics functional adaptation, anisotropy and seeds of micromechanics. Ph.D. thesis, Ben-Gurion University of the Negev, Beer-Sheva, Israel
30. Delfino A (1996) Analysis of stress field in a model of the human carotid bifurcation. Ph.D. thesis, Federal Institute of Technology, Lausanne, Switzerland
31. Hariton G, deBotton I, Gasser TC (2007) Holzapfel, stress-modulated collagen fiber remodeling in a human carotid bifurcation. J Theor Biol 248:460–470
32. Sommer G, Regitnig P, Költringer L, Holzapfel GA (2010) Biaxial mechanical properties of intact and layer-dissected human carotid arteries at physiological and supra-physiological loadings. Am J Physiol 298:H898–H912
33. Holzapfel GA, Ogden RW (2009) On planar biaxial tests for anisotropic nonlinearly elastic solids a continuum mechanical framework. Math Mech Solids 14:474–489
34. Chuong CJ, Fung YC (1986) On residual stress in arteries. J Biomech Eng 108:186–192
35. Takamizawa K, Hayashi K (1988) Uniform strain hypothesis and thin-walled theory in arterial mechanics. Biorheology 25:555–565
36. Vaishnav RN, Vossoughi J (1983) Estimation of residual strains in aortic segments. In: Hall CW (ed) Biomedical Engineering. II. Recent Developments. Pergamon, New York, pp 330–333
37. Greenwald SE, Moore JEJ, Rachev A, Kane TP, Meister JJ (1997) Experimental investigation of the distribution of residual strains in the artery wall. J Biomech Eng 119:438–444
38. Rachev A (2003) Remodeling of arteries in response to changes in their mechanical environment. In: Holzapfel G, Ogden R (eds) CISM course and lectures 441: biomechanics of soft tissue in cardiovascular systems. Springer-Verlag, Wien, pp 221–271
39. Holzapfel GA, Gasser TC, Ogden RW (2004) Comparison of a multi-layer structural model for arterial walls with a fung-type model, and issues of material stability. J Biomech Eng 126:264–275
40. Rhodin JG (1980) Architecture of the vessel wall. In: Bohr DF, Somlyo AD, Sparks HV (eds) Handbook of physiology. The cardiovascular system. Vol 2: vascular smooth muscle. American Physiological Society, Bethesda, pp 1–31
41. Demiray H, Vito RP (1991) A layered cylindrical shell model for an aorta. J Biomech 5:309311
42. Wang C, Garsia M, Lu X, Lanir Y, Kassab GS (2006) Three-dimensional mechanical properties of porcine coronary arteries: a validated two-layer model. Am J Physiol 291:H1200–H1209
43. Holzapfel GA (2000) Nonlinear solid mechanics: a continuum approach for engineering. Wiley, New York
44. Humphrey JD, Strumpf RK, Yin FCP (1990) Determination of a constitutive relation for passive myocardium: I. a new functional form. J Biomech Eng 112:333–339
45. Holzapfel GA, Gasser TCSM (2002) A structural model for the viscoelastic behavior of arterial walls: continuum formulation and finite element analysis. Eur J Mech A/Solids 21:441–463
46. Freed AD, Einstein AD, Vesely I (2005) Invariant formulation for dispersed transverse isotropy in aortic heart valves. An efficient means for modeling fiber splay. Biomech Model Mechanobiol 4:100117
47. Holzapfel GA, Ogden RW (2010) Constitutive modelling of arteries. Proceedings of the Royal Society A 466:1551–1597
48. Stålhand J, Klarbring A, Karlsson M (2004) Towards in vivo aorta material identification and stress estimation. Biomech Model Mechanobiol 2:169–186
49. Stålhand J, Klarbring A (2005) Aorta in vivo parameter identification using an axial force constraint. Biomech Model Mechanobiol 3:191–199
50. Stålhand J, Klarbring A (2006) Parameter identification in arteries using constraints. In: Holzapfel GA, Ogden RW (eds) Mechanics of biological tissues. Springer, Wien, pp 295–305
51. Canham PB, Talman EA, Finlay HM (2001) Medial collagen organization in human arteries of the heart and brain by polarized light microscopy. Connect Tissue Res 26:121–134
52. Finlay HM, McCullough L, Canham PB (1995) Three-dimensional collagen organization of human brain arteries at different transmural pressures. J Vasc Res 32:301–312
53. Sommer G, Holzapfel GA (2012) 3d constitutive modeling of the biaxial mechanical response of intact and layer-dissected human carotid arteries. J Mech Behav Biomed Mater 5:116128
54. Sommer G (2008) Mechanical properties of healthy and diseased human arteries. Ph.D. thesis, Graz University of Technology, Institute of Biomechanics
55. Ogede RW, Saccomandi G, Sgura I (2004) Fitting hyperelastic model to experimental data. Comput Mech 34:484–502
56. Cortes DH, Lake SP, Kadlowec JA, Elliot DM (2010) Characterizing the mechanical contribution of fiber angular distribution in connective tissue: comparison of two modeling approach. Biomech Model Mechanobiol 9:651658
57. Wang C, Guo X, Kassab GS (2009) A new observation on the stress distribution in the coronary artery wall. J Biomech Eng. doi:10.1115/1.4000106
58. Stylianopoulos T, Barocas VH (2007) Multiscale, structure-based modeling for the elastic mechanical behavior of arterial walls. J Biomech 129:611–618
59. Maceri F, Marino M, Vairo G (2010) A unified multiscale mechanical model for soft collagenous tissues with regular fiber arrangement. J Biomech 43:355–363